Materials Science & Engineering B 227 (2018) 39–47

Contents lists available at ScienceDirect

Materials Science & Engineering B

journal homepage: www.elsevier.com/locate/mseb

Application of FORC distributions to the study of magnetic interactions in Co-doped $BaTiO_3$ nanomaterials

S. Fuentes[a,f,*], H. Pizarro[b,c], P. Gutiérrez[b], D.E. Diaz-Droguett[d,g], N. Barraza[e]

[a] Departamento de Ciencias Farmacéuticas, Facultad de Ciencias, Universidad Católica del Norte, Casilla 1280, Antofagasta, Chile
[b] Laboratorio de Magnetismo, Departamento de Ciencias Geológicas, Universidad Católica del Norte, Antofagasta, Chile
[c] Géosciences Environnement Toulouse, Université Toulouse III-Paul Sabatier, Toulouse, France
[d] Instituto de Física, Facultad de Física, Pontificia Universidad Católica de Chile, Casilla 306, Santiago, Chile
[e] Departamento de Física, Facultad de Ciencias, Universidad de Santiago de Chile, Casilla 9170124, Santiago, Chile
[f] Center for the Development of Nanoscience and Nanotechnology, CEDENNA, Santiago, Chile
[g] Research Center for Nanotechnology and Advanced Materials, CIEN-UC, Santiago, Chile

ARTICLE INFO

Keywords:
Magnetic properties
$BaTiO_3$
Co-doping
Oxidation states

ABSTRACT

Co-doped $BaTiO_3$ (BT) nanomaterials were synthesized by a combination of sol-gel and hydrothermal methods under an oxygen partial pressure of 200 psi. The surface chemistry of the samples and, in particular, the oxidation state of the Co atoms, was investigated by X-ray photoelectron spectroscopy, while X-ray powder diffraction and Raman spectroscopy were used to obtain structural information. Morphological information was acquired by atomic force microscopy. The dependence of the magnetic properties of the samples as a function of Co-doping level in BT and the effect of the base used in the synthesis of the compound (i.e. NaOH or KOH) was studied from the analysis of hysteresis curves and FORC diagrams. The results demonstrated that the level of ferromagnetic component tend to increases as the percentage of Co doping is decreased.

1. Introduction

Multiferroics are considered as one of the prominent classes of multifunctional materials since possess two or more ferroic properties which generally refer to the coexistence of ferroelectric and ferromagnetic properties [1,2].

Although the mutual control of electric and magnetic properties is an attractive possibility, the number of candidate materials in this respect is currently limited, as the preparation of multiferroic materials is not an easy task. Many factors such as symmetry, electronic properties, chemistry and structure (i.e. grain size, crystal quality, microstructure, crystallographic orientation, defects and domains structure) must be taken into account [3,4]. In particular, interest has been focused on the development of compounds with the perovskite crystal structure of $BaTiO_3$ (BT), which is intentionally doped with 3*d* transition metals, such as Co, Ni and Fe, aiming to form multifunctional materials with potential applications in the emerging fields of spintronics, data-storage media and multiple-state memory cells [5–7]. BT has been one of the best known and widely used materials for electric ceramics due to its excellent dielectric, ferroelectric and piezoelectric properties [8–9]. According to *Mangalam et al.*, ferroelectricity in BT arises from the off-centring of Ti ions with respect to a centrosymmetric cubic perovskite crystal [10].

Several groups have reported room-temperature ferromagnetism in Co-doped BT and similar perovskite oxides, but the cobalt oxidation state is not mentioned, and is usually assumed to be located inside the BT lattice as Co^{2+} [11–13]. The Co oxidation state is important in revealing more about the chemical composition of BT when doped and the possible substitution mechanisms when Co is incorporated inside the BT structure. A theoretical study by *Nakayama et al.* has indicated that Cr, Mn, Fe and, most likely, Co are the most suitable dopants for achieving ferromagnetism in BT compounds [14]. However, to date, no one has presented convincing evidence indicating that the observed ferromagnetism is intrinsic. Thus, the intrinsic nature of magnetism of metal-doped BT remains an open question.

To help answer this question, First Order Reversal Curves (FORC) diagrams can be used, which is a powerful method of investigating hysteresis in magnetic systems and has been widely applied to different systems [15,16]. A FORC diagram contains much more detailed information about hysteresis properties than the major hysteresis loops or the remanence curves. It can be used to probe subtle variations in magnetic properties that might not be noticed with conventional hysteresis measurements. Thus, the experimental measurement of FORC diagrams, performed to obtain magnetization as a function of the

* Corresponding author at: Departamento de Ciencias Farmacéuticas, Facultad de Ciencias, Universidad Católica del Norte, Casilla 1280, Antofagasta, Chile.
E-mail address: sfuentes@ucn.cl (S. Fuentes).

http://dx.doi.org/10.1016/j.mseb.2017.10.010
Received 15 June 2017; Received in revised form 5 October 2017; Accepted 11 October 2017
Available online 17 October 2017
0921-5107/

reversal field Hr and the applied field H, is becoming an essential tool to characterize the hysteretical behavior of ferromagnetic particles, and to investigate their intrinsic magnetic interactions [17,18].

In this paper, we apply the FORC method to study Co-doped BT nanomaterials synthesized by a combined sol-gel-hydrothermal method using two different bases (i.e. NaOH and KOH) under an oxygen atmosphere. The effects of the synthesis conditions and chemical composition on the characteristics of resulting compound are analyzed, including the structural phase, oxidation states and magnetic modifications.

2. Experimental

2.1. Materials

Tetrabutyl titanate (*TBT*, *97%*), Chloride barium ($BaCl_2$, 99.999%), Cobalt(II) chloride hexahydrate ($CoCl_2{\cdot}6H_2O$, 99%), Sodium hydroxide (NaOH, ≥98%) and Potassium hydroxide (KOH, 90%) were purchased from Sigma–Aldrich as starting materials.

2.2. Synthesis

$BaTi_{1-x}O_3$:Co_x powders with x = 0, 1, 3 and 5 mol% Co as their nominal dopant ion concentrations, were synthesized by the sol-gel-hydrothermal process using tetrabutyl titanate (TBT), chloride barium ($BaCl_2$) and cobalt chloride ($CoCl_2$) as starting materials. In a typical procedure, solution (A) containing 1 mL of TBT was diluted with 8.2 mL of ethanol for 10 min to form a white solution, which was added dropwise at 60 °C for 3 h with stirring to solution (B), which contained 1 mL of HNO_3 in 39 mL of deionised water (45 °C). Aqueous solution (C) was prepared by dissolving $BaCl_2$ in 4 mL of deionised water, and solution (D) was prepared by dissolving $CoCl_2$ in 2 mL of deionised water.

To prepare the $BaTi_{1-x}O_3$:Co_x precursor, solutions (C) and (D) were added dropwise to solution (B). Under stirring and N_2 bubbling, NaOH or KOH was added to the barium cobalt titanium solution, and a white homogeneous colloidal barium cobalt titanium slurry was formed.

The mixed solution was transferred to a 500 mL Teflon-lined stainless steel reactor, sealed and then heated at 180 °C for 24 h under an oxygen partial pressure of 200 psi. At the end of the reaction, the autoclave was allowed to cool to room temperature. The as-synthesized white powder attached to the bottom and inner wall of the Teflon container was collected, centrifuged, washed with distilled water and ethanol to remove the remaining ions and dried at 60 °C for 6 h under reduced pressure.

2.3. Characterization

Surface chemical information about the Co-doped BT samples was obtained by X-ray photoelectron spectroscopy (XPS; Physical Electronics system model 1257) using Al K_α emission. The binding energies and oxidation states were obtained from high-resolution scans. The energy scale was calibrated by assigning 284.8 eV to the C 1s peak, corresponding to adventitious carbon. X-ray diffraction (XRD) data were acquired using a Siemens Advanced D-8 diffractometer with CuK_α radiation at 40 kV and 30 mA. Raman spectra were recorded on a WITEC model CRC200, using a 5.5 mW laser with a wavelength of 514.5 nm. AFM images were obtained in contact mode with Si_3N_4 tips using the same equipment (WITEC model CRC200). The magnetic properties were performed at room temperature (25 °C) using a Magnetometer MicroMag 2900-2 from Princeton Measurement Corporation, with an alternative gradient magnetometer (AGM). The FORCs were processed with the free software FORCinel, which is widely used to process FORCs [19–21]. The hysteresis curves were analyzed by Micromag AGM and PmagPy (Tauxe, 1198) softwares.

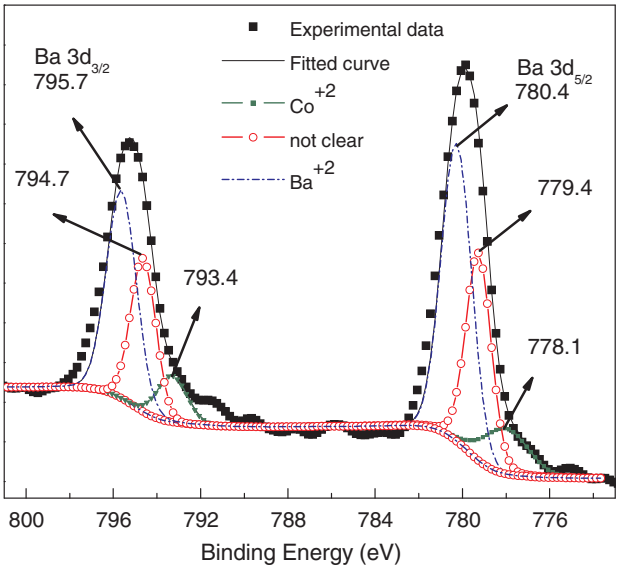

Fig. 1. High resolution XPS spectrum of the 802–773 eV spectral range acquired from the 3 mol% Co-doped BT nanoparticles grown using KOH.

3. Results and discussion

3.1. Surface chemical characterization

The XPS spectra obtained were used to determine the surface chemistry characteristics of the samples and, in particular, the oxidation state of the Co atoms. A representative high-resolution XPS spectrum from the 802–773 eV spectral range is shown in Fig. 1., acquired from the nominal 3 mol% Co-doped BT sample grown using KOH.

Each main peak was fitted using three curves. The binding energies (BEs) of 780.4 eV (Ba $3d_{5/2}$) and 795.7 eV (Ba $3d_{3/2}$) are associated with Ba^{2+} ions in non-perovskite structure of BT compound since the BEs of Ba^{2+} in a BT perovskite structure have slightly lower values (i.e. ~779.4 eV and ~794.4 eV) as reported in references [22–24]. The curves with BEs shifted to the lowest values of 778.1 eV and 793.4 eV are attributed to the presence of Co^{2+} ions. The BEs of 779.4 eV and 794.7 eV and their energy difference of 15.3 eV are difficult to interpret. This is because the peak centred at 779.4 eV can be attributed to either the presence of Co^{3+} ions or the presence of Ba^{2+} ions in a BT perovskite structure. The other possibility is that this peak (779.4 eV) might correspond precisely to both the presence of Ba^{2+} ions in a BT perovskite structure and the presence of Co^{2+} ions but, in this case, with a different chemical environment inside the BT lattice as compared to the Co^{2+} ions of 778.1 eV of binding energy. The same interpretation, therefore, could be assigned to the peak centred at 794.7 eV. The assignment of this spectral zone (802–773 eV) matches with the assignment performed by *Norman et al.* [24] and *Jung et al.* [25], who studied the compound $Ba_{0.5}Sr_{0.5}Co_xFe_{1-x}O_{3-\delta}$ by XPS. However, our BE values related to the possible presence Co^{3+} and to the presence of Co^{2+} ions are lower than those reported by these authors. A more precise interpretation of these XPS signals and of the peaks centred at 779.4 eV and 794.7 eV in particular, requires further investigation. By way of comparison, Table 1 summarises the values of BEs observed in the sample grown under the same conditions but using a NaOH base, to evaluate its effect on the determined binding energies. The XPS spectrum was also fitted using the three curves for each peak.

The possible presence of Co^{3+} ions could be explained by the substitution of some Ti^{4+} ions (B-sites) by Co^{3+} ions during the doping. A substitution of Ba^{2+} (A-sites) by Co^{3+} is less probable due to the large difference between their ionic radii i.e. 1.4 Å for Ba^{2+} and 0.5 Å for Co^{3+}. Co^{2+} ions may substitute for some Ti^{4+} ions (B-sites) as well as some Ba^{2+} ions (A-sites) in the BT lattice. In the case of the substitution

Table 1
Binding energy values obtained from the curve fit for the 3 mol% Co-doped BT nanoparticles grown using NaOH base.

Ion in Co-doped BT structure	Binding Energy (eV)
Ba^{2+}	780.3 ($3d_{5/2}$); 795.6 ($3d_{3/2}$)
Co^{2+}	778.1 ($2p_{3/2}$); 793.3 ($2p_{1/2}$)
Not clear	779.2 ($2p_{3/2}$); 794.5 ($2p_{3/2}$)

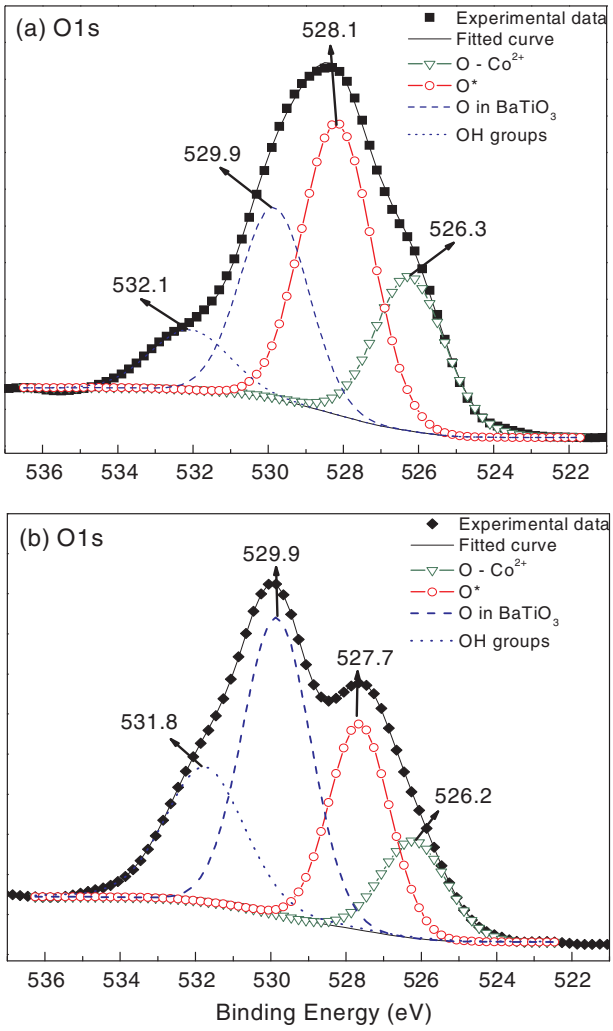

Fig. 2. High resolution XPS spectra of O1s level acquired from 3 mol% Co-doped BT nanoparticles prepared with a) NaOH base and b) KOH.

of isovalent ions, such Ba^{2+} by Co^{2+}, the substitution would lead to a high strain of the BT lattice due to the large difference in their ionic radii (0.9 Å for Co^{2+}). On the other hand, the substitution of some Ti^{4+} by Co^{2+} would produce a minor lattice strain because the ionic radii of the species are more similar (0.6 Å for Ti^{4+}), where the charge difference should be compensated, for example, by the creation of an oxygen vacancies inside the BT lattice.

Fig. 2 shows high-resolution XPS spectra of the O1s level and fitted curves acquired from two samples grown under the same preparation conditions but with different bases for comparison. Fig. 2(a) corresponds to the sample nominal 3 mol% Co-doped BT grown using NaOH, and Fig. 2(b) corresponds to the sample nominal 3 mol% Co-doped BT using KOH. Both spectra were fitted using four curves. The BEs of 526.3 eV and 526.2 eV were attributed to oxygen bound to Co^{2+} ions. The values of 528.1 eV and 527.7 eV were attributed to oxygen (O^{*}) with the possible presence of Co^{3+} or Co^{2+} ions in another chemical state, or oxygen bound to Ba^{2+} in a perovskite chemical environment. The BEs values of 529.9 eV in both cases (Fig. 2(a) and (b)) correspond to O^{2-} ions related to oxygen in a BT non-perovskite structure. The fourth curve at the highest binding energy (532.1 eV and 531.8 eV) is attributed to chemisorbed species on the surface such as hydroxyl (OH) groups. However, the contribution from some oxygen vacancies present in the BT structure for these signals at 532.1 eV and 531.8 eV is not ruled out. Our BE values associated with oxygen in the BT structure are very similar to the values reported by *Nasser et al.* [22] and to the values reported for oxygen inside a $Ba_xSr_{1-x}TiO_3$ structure [26,27].

Therefore, the base (NaOH or KOH) influence on the chemical characteristics of the oxygen present, as revealed by the oxidation states O^{2-}, O^{*} and OH groups found in the nominal 3 mol% Co doped BT samples. The sample prepared in KOH shows the presence of oxygen in state O^{2-} and OH groups is major that the samples prepared in NaOH.

Thus, KOH would induce more defects and the presence of chemisorbed species in the samples. On the other hand, the presence of the O^{2-} ions related to oxygen in a BT non-perovskite structure is major in KOH.

3.2. Structural characterization

Fig. 3 shows the XRD patterns of the BT and Co-doped BT samples synthesized with the two different bases (NaOH and KOH). As shown in Fig. 3(a) (NaOH) and Fig. 3(b) (KOH), the sharp and well-defined peaks reveal high crystallinity for all as-prepared Co-doped BT powders, which were not submitted to any heat treatment. The XRD Bragg reflection was assigned to that of a cubic perovskite structure of Co-doped BT. In fact, all of the main peaks for the Co-doped BT samples shown in Fig. 3 are apparently stabilised in the cubic lattice (space group *Pm3m*) for the BT powders at room temperature. The calculated lattice constants are in agreement with the tabulated values of a = 4.0260 Å; JCPDS card No. 31-0174.

The average particle size was estimated from (1 1 7) diffraction peak and the Scherrer equation given by: $d = k\lambda/(\beta/\cos(\theta))$, where d is particle size, $k \sim 1$ is the shape factor, $\lambda = 0.1540$ nm is the wavelength of the CuKα radiation, β is the full-width at half-maximum (FWHM) and θ is the diffraction angle. The average grain sizes of the Co-doped BT in NaOH and KOH are 70.4 nm and 88.1 nm respectively.

Fig. 4(a) (NaOH) and 4(b) (KOH) show the XRD patterns of BT and Co-doped BT in the 44–46° 2Θ range for all of the samples. The effect of Co substitution on the BT structure can be observed by the clear shift in the (2 0 0) reflection, which is characteristic of the cubic lattice of Co-doped BT. For each method used to prepare the Co-doped BT samples, splitting of the (2 0 0)/(0 0 2) diffraction peaks was not observed, indicating that the samples were stabilised in the cubic phase at room temperature [12]. The shift in the strongest diffraction peak (*hkl*) with respect at BT is closely associated with the ionic radii of Co^{2+}, Co^{3+}, Ba^{2+} and Ti^{4+}. According to *Shannon et al.* [28], the ionic radii are 1.42 Å for Ba^{2+}; 0.9 Å for Co^{2+}; 0.53 Å for Co^{3+}; and 0.605 Å for Ti^{4+}. The coordination numbers of Ti^{4+}/Co^{3+} and Ba^{2+}/Co^{2+} in the structure are 6 and 12, respectively.

According to *Cui et al.* [29], Co^{2+} ions are more likely to replace Ti^{4+} ions due to their similar ionic size. When Co^{2+} ions substitute into Ti^{4+} sites, the resulting negative charge must be compensated for by oxygen vacancies. If Co^{2+} substitutes into both positions, self-compensation could occur. Our results suggest that Co^{2+} replaces the Ti^{4+} sites at low concentration nominal (1 and 3 mol%), whereas both sites, Ba^{2+} and Ti^{4+}, may be substituted with Co^{3+} ions when the concentration increases (i.e. 5 mol%). When Co^{2+} replaces Ti^{4+} in the structure, expansion of the crystal lattice takes place, whereas when Co^{3+} ions replace both Ba^{2+} and Ti^{4+}, it is possible obtain a small lattice distortion that explains the shift to higher values of 2Θ. The presence of Co in two oxidation states (Co^{3+} and Co^{2+}) and the possible substitution due to Co doping is also supported by our XPS results.

In contrast to the XRD technique, Raman spectroscopy is a highly

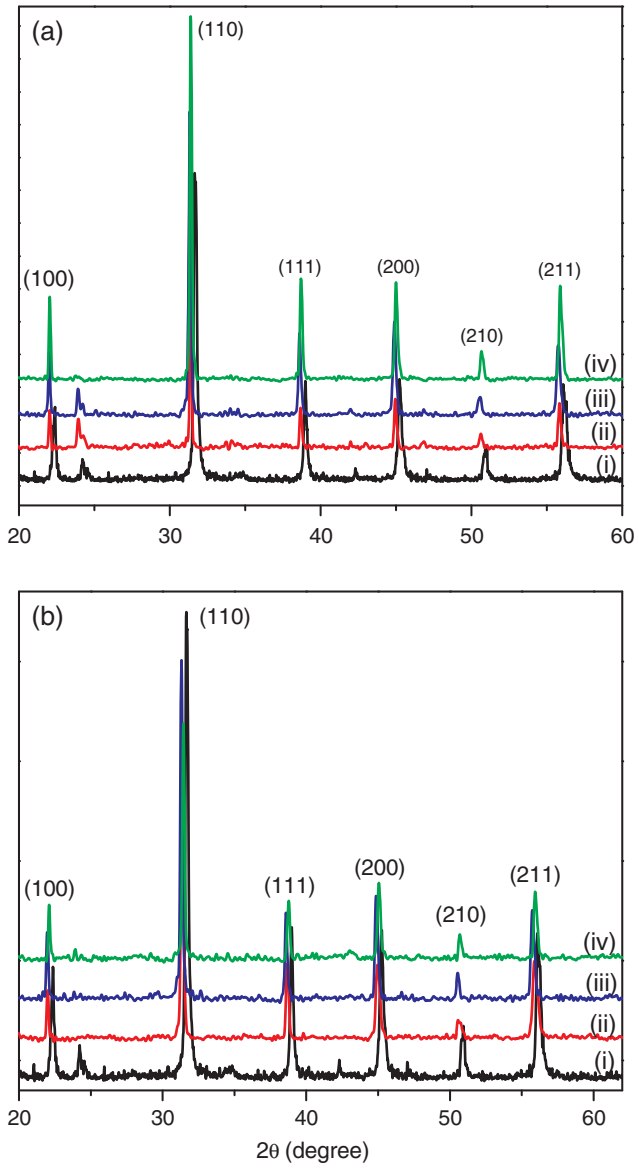

Fig. 3. XRD patterns of the BT nanoparticles prepared with (a) NaOH and (b) KOH, doped with different content of Co: (i) 0%, (ii) 1%, (iii) 3% and (iv) 5 mol%.

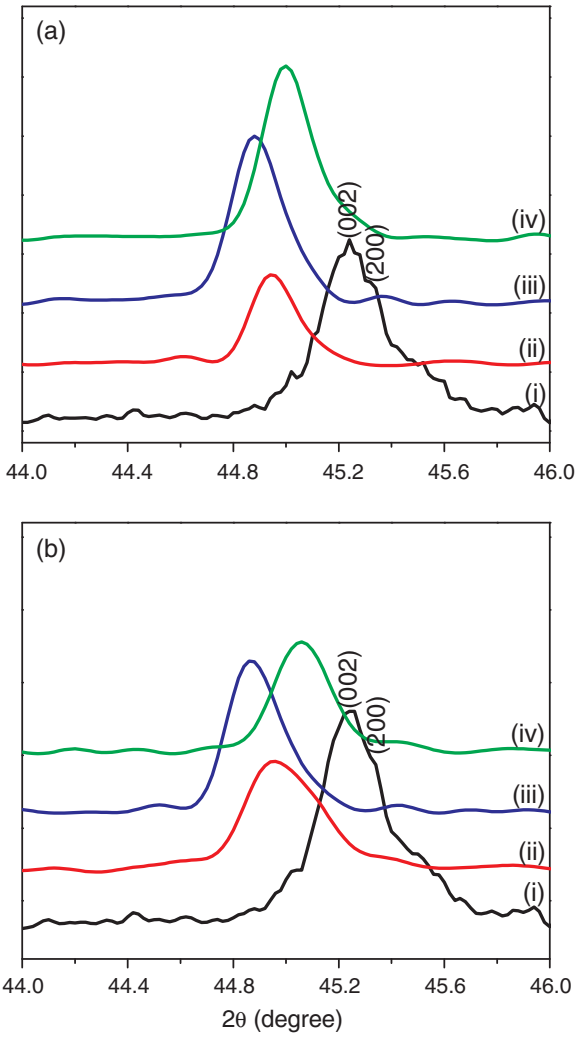

Fig. 4. XRD patterns in the 2Θ region of 44 and 46° of the BT nanoparticles prepared with (a) NaOH and (b) KOH, doped with different content of Co: (i) 0%, (ii) 1%, (iii) 3% and (iv) 5 mol%.

sensitive technique to probe the local structure of BT samples. BT single crystals at room temperature have a tetragonal perovskite structure (space group *P4mm*) with one formula unit per unit cell. Only below the Curie point, near 120 °C, does BT become ferroelectric. In the interval 120–1460 °C BT monocrystals take the paraelectric cubic perovskite structure (space group *Pm3m*).

The Raman spectra obtained at room temperature for Co-doped BT synthesized in NaOH and KOH are shown in Fig. 5(a) and (b), respectively. The Raman spectra of the BT samples prepared in both bases are similar to those obtained for nanoparticles of pure BT analyzed in a previous study [30]. They present a characteristic Raman peak near 306 cm^{-1} (B1 mode) corresponding to the tetragonal BT phase and contradict the cubic symmetry observed by XRD analysis from which no first-order Raman activity is expected. *Busca* et al. [31] reported a distortion of the TiO_6 octahedron in the cubic BT phase inducing a pseudotetragonality of the cubic phase. This could explain the significantly lower symmetry with respect to a cubic perovskite structure, similar to that of the tetragonal BT.

In general, four characteristic Raman bands are present in the samples at approximately 306 cm^{-1} [B_1, E(TO + LO)], and broad bands near 268 cm^{-1} [A_1(TO)], 519 cm^{-1} [A_1, E(TO)] and 720 cm^{-1} [A_1, E(LO)] are observed.

The cubic phase of this polymorph, which does not reveal Raman active modes, generally shows broad bands at around 250 and 520 cm^{-1}, which may be caused by local disorder associated with the position of Ti atoms. On the other hand, with increasing Co, the intensities of the Raman peaks change. The bands associated with the tetragonal perovskite structure exhibit a decrease in intensity; this is caused by the tetragonal-to-cubic phase transition from BT to Co-doped BT and is consistent with the effect observed by X-ray diffraction analysis.

The band at approximately 250 cm^{-1} for BT shows a continuous increase, whereas the band at approximately 520 cm^{-1} shifts to lower frequencies (515 cm^{-1}); furthermore, the intensity of the band decreased with mol% Co. The characteristic band at 720 cm^{-1} shows a minor relative intensity for doped BT compared with the band for undoped BT, which can be ascribed to defects in the BT lattice [31].

The morphology of the samples was analyzed by atomic force microscopy (AFM). The AFM images of the naked nominal 5 mol% Co-doped BT nanoparticles in NaOH and KOH are shown in Fig. 6(a) and (b), respectively. In general, the samples prepared using both bases exhibit agglomerates, almost spherical in shape, with diameters of approximately 120 nm and 250 nm, respectively. Through the application of ultrasonic agitation for 10 min for 40 kHz ultrasonic

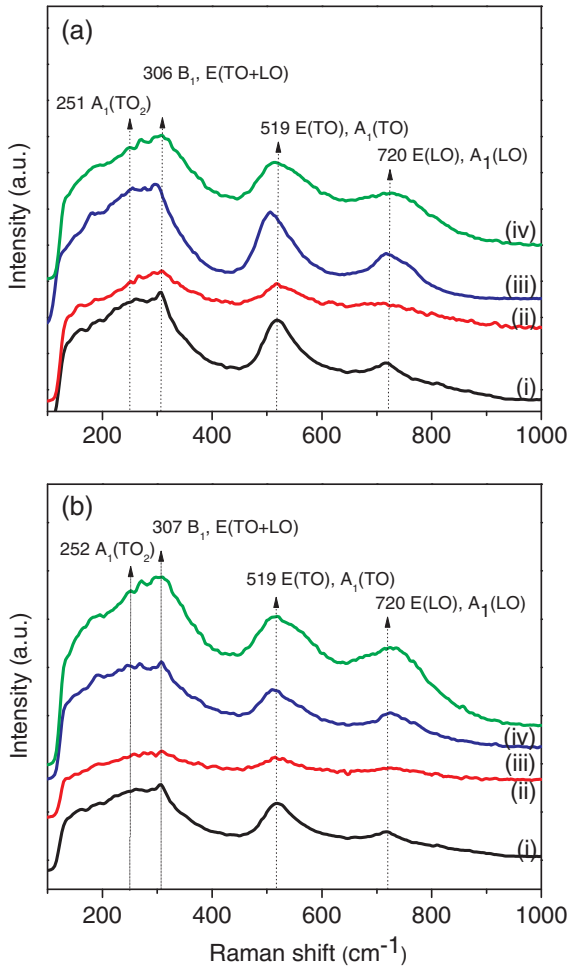

Fig. 5. Raman spectra of BT nanoparticles prepared with (a) NaOH and (b) KOH, doped with different content of Co: (i) 0%, (ii) 1%, (iii) 3% and (iv) 5 mol%.

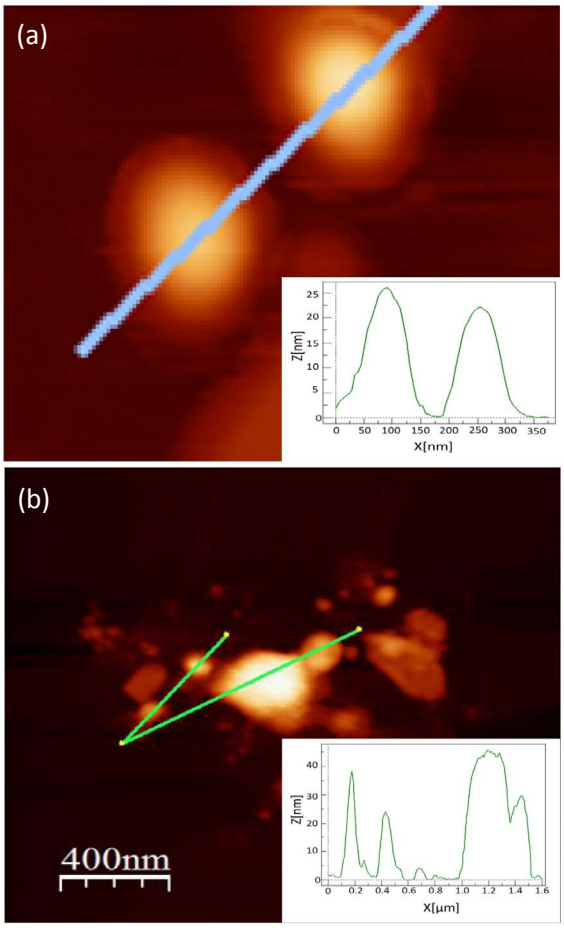

Fig. 6. Acustic AFM images of 5 mol% Co-doped BT nanoparticles prepared with (a) NaOH and (b) KOH. The *inset* shows the particles size distribution histogram.

wave, we obtained the particle size distribution histogram as is shown in the inset of the corresponding AFM images.

3.3. Magnetic properties

Fig. 7 shows hysteresis curves measured at room temperature of BT and Co-doped BT samples (nominal 1, 3 and 5 mol%) synthesized using NaOH and KOH, each concentration was measured 6 times. From these curves, different behaviors can be observed. The nominal 5 mol% Co-doped BT samples in NaOH and KOH mainly exhibit paramagnetic behavior, which is shown by the shape of the curves in addition to the high values of high-field magnetic susceptibilities (χ_{hf}) and high and low-field susceptibility ratios (χ_{hf}/χ_{lf}) (see Table 2). In addition, both samples also present a weak ferromagnetic behavior denoted by the low values in the magnetic parameters of magnetic saturation (M_s) and magnetic remanence (M_r). On the other hand, Co-doped BT synthesized using NaOH (nominal 1 and 3 mol%) and KOH (nominal 3 mol%) exhibit a paramagnetic and ferromagnetic behavior, but in this case with a greater ferromagnetic contribution compared to the previous case. This is evidenced by the curve's shape, lower values of χ_{hf} and χ_{hf}/χ_{lf}, and higher values of M_r and coercive field (H_c), than the previous samples doped with nominal 5 mol% (Table 2). Finally, the sample doped at nominal 1 mol% synthesized using KOH exhibits strong ferromagnetic behavior which is evident from high values of χ_{lf}, χ_{ferri}, M_s and M_r, and low (or negative) values of χ_{hf} and χ_{hf}/χ_{lf}. However, these last negative values could be also due to a weak diamagnetic contribution.

From the hysteresis curves data, it is also possible to determinate the magnetization ratio, which is calculated by the ratio of *Mr/Ms*. This value corresponds to a measure of the "magnetic memory", accounting for the percentage of retainer magnetization. In this way, for example, it can be observed that the nominal 5 mol% Co-doped BT sample in both KOH and NaOH, presents lower values, which is consistent with the paramagnetic behavior inferred from the magnetic properties. It has been established that this capacity to retain magnetism is strongly linked to the favorable magnetic size of the particles in a sample [32]. Thus, the values of magnetic properties of different materials may be used to determine the magnetic size of particles and thereby infer the magnetic domain prevailing in a sample.

On the other hand, the paramagnetic behavior in nominal 5 mol% Co doped BT may be due to a similar behavior to that presented with the ferrites (MFe_2O_4, M represents a metal cation), where the oxidation state of the Fe atoms can be Fe^{2+} or Fe^{3+}. In the cubic ferrites, the magnetic moments of the Fe^{3+} ions in octahedral position cancel with the magnetic moments of the Fe^{3+} ions in the tetrahedral position, the net result is the cancellation of the magnetic moment by virtue of the antiparallel coupling shown. The net magnetic moment is attributed only to the Fe^{2+} ions which are aligned in the same direction. In our case, the Raman spectra shows that with the increase of the mol% of Co ions, the bands associated with the tetragonal perovskite structure exhibit a decrease in intensity (307 cm^{-1}); this is caused by the tetragonal-to-cubic phase transition from BT to Co-doped BT. Therefore, there could be two reasons that explain the paramagnetic behavior of cobalt ions: the existence of Co^{3+} ions and the phase change to a cubic structure from a pseudo tetragonal.

To determine the magnetic domains (i.e. magnetic grain size) within the BT nanoparticles, magnetization (M_r/M_s) and coercivity (H_{cr}/H_c)

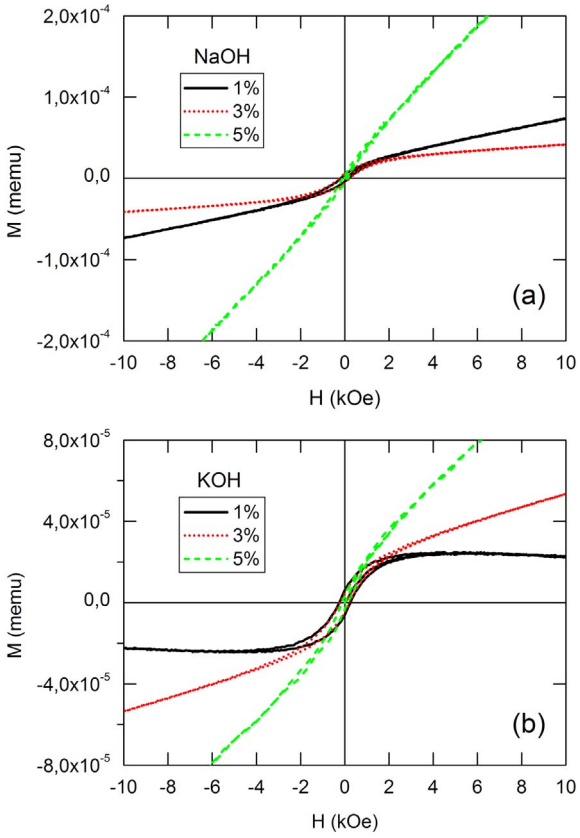

Fig. 7. Measured hysteresis cycles of the BT nanoparticles prepared with (a) NaOH and (b) KOH, doped with different content of Co: 1%, 3% and 5 mol%.

ratios were used, following *Day* et al. whose values were plotted in the Theoretical Day plot in Dunlop [33,34]. In Fig. 8 it can be seen that the plotted values are in the pseudo-single-domain (PSD) field between single-domain (SD) + multi-domain (MD) mixing curves and SD + superparamagnetic (SP) (10 nm) domain mixing curve, relatively close to each other. This disposal is likely due a mixture of PSD and SP grains or a ternary mixture of SP + SD + MD [35]. The samples doped at nominal 5 mol% in NaOH are plotted relatively far from the SD + SP (10 nm) mixing curve, showing a PSD predominance over the SP and SD domains. On the other hand, the samples doped at nominal 1 and 3 mol% in both KOH and NaOH and the sample doped at nominal 5 mol % in KOH, are plotted in the PSD range close to the SD + SP (10 nm) curves. Thus, from the magnetic properties (i.e. high values of magnetization and coercitivity), suggest that these samples consist mainly of PSD and/or SP domains.

As can be seen from the above, valuable information can be obtained from hysteresis curve analysis relating to the properties of a system composed of numerous particles such as: χ_{hf}, H_c, M_s, M_r, *Ms/Mr.* and *Hcr/Hc*, among others. However, with this previous analysis, it is not possible to clarify all aspects of a many-particle system. The FORC (first-order reversal curves) diagram technique is a powerful tool for the characterization of magnetic systems composed of many nanoparticles [36,37]. This technique has been used to study magnetic properties in greater detail to determine the possible distributions of coercivity, interaction fields and the levels of reversible and irreversible magnetization in the samples [15,38–41]. Additionally, the FORC diagrams can be used to discriminate between different types of magnetic behavior. It can also discriminate between mixtures of grains with variable domain states (e.g. size distribution of the particles) and identify the presence or absence of magnetostatic interaction. This is because grains with different domain structures and interactions plot in different parts of the FORC diagrams [15,16].

The measurement of a FORC begins by saturating the sample at a high external field, thus reaching the *Ms.* of the sample. The external field is then reduced to a *Ha* magnetic field, known as the reversion or initial field. The FORC is defined as the magnetization curve (within the hysteresis loop) that ranges from the initial *Ha* field to saturation. Magnetization in the external *Hb* field on the FORC with the initial *Ha* field is denoted by *M(Ha,Hb)*, where $Hb > Ha$. The information obtained using FORCs is interpreted through a statistical model based on the Preisach model [38], which describes a magnetic system as a set of magnetic entities termed histerions, each one of which contributes to the system with a statistical value defined by the probability density function of the ensemble. The probability density function of the ensemble is defined by:

$$\rho(H_a,H_b) = -\frac{1}{2}\frac{\partial^2 M}{\partial H_a \partial H_b} \quad (1)$$

Where; $M = M(Ha, Hb)$, $\rho(Ha, Hb)$ extends over the entire *Ha*, *Hb* plane. Thus, the FORC diagram is a contour plot of the probability density function of the ensemble, ρ, which can be expressed in terms of the variables $Hcf = (Hb - Ha)/2$ and $Hu = (Hb + Ha)/2$. These variables represent the switching (coercivity of an entity) and interaction fields (a shift in the hysteresis curve of an entity), which have a more direct and intuitive physical interpretation [20]. This change of variables allows us to capture the component of reversible magnetization that appears at $Hcf = 0$ and the irreversible magnetization component (s) of the system for $Hcf > 0$. The density function ρ is obtained from the numerical derivation of the function *M(Ha,Hb)*, which contains all of the FORC measurements. Finally, the FORC diagram is obtained using a contour plot of the *Hcf*, *Hu* function.

Fig. 9 shows the FORC diagrams of the Co-doped BT (nominal: 1, 3 and 5 mol%) samples synthesized with NaOH and KOH. The first characteristic that stands out in the FORC diagrams is the similarity of the ρ function, with the exception of the samples with a Co-doped nominal 5 mol% (NaOH and KOH), which had increased noise in the magnetic signal (see Fig. 7 and Table 2), thus making it difficult to obtain a set of well-defined FORCs. It is also possible to observed two magnetic phases in the samples, (except in NaOH (Co-doped 5 mol%)), one centred on $Hcf = 0$ and $Hu < 0$, which corresponds to the reversible magnetization component associated with paramagnetic materials and the other centred on $Hcf > 0$ and $Hu > 0$, which corresponds

Table 2
Magnetic properties of the Co-doped BT nanoparticles.

Mol% Co	Susceptibilities (m^3/kg)			Remanences (memu/g)		Coercivities (Oe)		Ratios		
	χ_{hifi}	χ_{if}	χ_{ferri}	Ms	Mr	Hc	Hrc	χ_{hifi}/χ_{if}	Mr/Ms	Hcr/Hc
1%	2.98E−09	8.67E−09	5.69E−09	0.79	0.17	229.1	871	0.34	0.22	3.8
NaOH 3%	2.52E−09	2.29E−08	2.03E−08	2.86	0.71	254.1	814	0.11	0.25	3.2
5%	8.56E−09	1.22E−08	3.64E−09	0.5	0.09	224.4	869	0.7	0.17	3.87
1%	−8.96E−10	2.56E−08	2.65E−08	3.79	0.84	246.2	808	−0.03	0.22	3.28
KOH 3%	3.10E−09	1.41E−08	1.10E−08	1.58	0.37	254.2	800	0.22	0.23	3.15
5%	8.38E−09	1.70E−08	8.60E−09	1.02	0.22	235.3	905	0.49	0.21	3.85

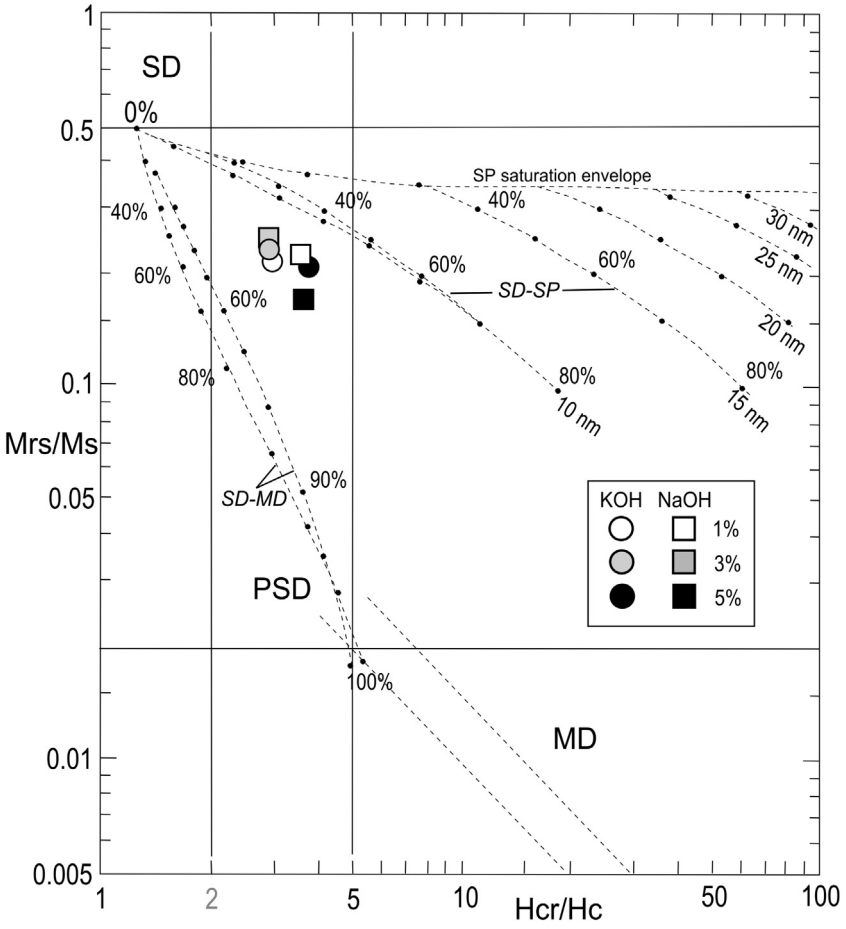

Fig. 8. Hcr/Hc logarithmic plot for representative BT nanoparticles samples prepared with NaOH and KOH doped with different content of Co (1, 3 y 5 mol%). The dashed lines represent mixing curves from for mixtures of single-domain (SD) with multidomain (MD) or superparamagnetic (SP) particles.

to the irreversible magnetization component associated with the ferromagnetic nanoparticles in the sample.

In Fig. 9a it is observed that the concentration of reversible magnetization component in the NaOH sample at nominal 1 mol% Co-doped BT is higher than the irreversible magnetization component, which is characteristic of a system in which the paramagnetic phase is predominant. In the NaOH sample at nominal 3 mol% Co-doped BT, the reversible magnetization component has a similar value to that of the ferromagnetic component, which describes a system with a ferromagnetic tendency. In both systems (NaOH at 1 and 3 mol% Co-doped BT) we observe that the ferromagnetic phase (centred in $Hcf > 0$ and $Hu > 0$) has a coercivity distribution (in the Hcf axis) that indicates a distribution of coercivities of the nanoparticles that is possibly due to size distribution [40,41]. Likewise, a distribution of interaction is observed in both systems, indicating the magnetic interaction among the nanoparticles due to the agglomeration. The ferromagnetic phases for the NaOH-grown samples at nominal 1 and 3 mol% Co are centred in Hcf = 274.14 Oe and 288.31 Oe which are very close to the values obtained by the hysteresis curves of Hc = 229.10 Oe and 254.10 Oe.

In Fig. 9b it is observed the FORCs diagrams of the samples prepared with KOH exhibit similar behavior as a function of doping (nominal 1, 3 and 5 mol% Co-doped BT). The samples that contain doping at nominal 3 and 5 mol% Co show a reversible magnetization component higher than the irreversible magnetization component, which is characteristic of a system in which the paramagnetic phase is predominant. In the KOH-grown sample at nominal 1 mol% Co the reversible magnetization component has a lower value than the irreversible magnetization component, which describes a system with a great ferromagnetic tendency. The width of the distribution of the coercivity of the ferromagnetic phase ($Hcf > 0$) in the three diagrams indicates that there is also a coercivity distribution associated with the size distribution of the particles. Likewise, the width of the distribution of the interaction of the ferromagnetic phase indicates that there is magnetic interaction among the nanoparticles owing to their agglomeration. The ferromagnetic (irreversible) component of the samples of KOH at nominal 1 and 3 mol% Co-are centred at Hcf = 286.79 and 290.90 Oe, respectively, values very similar to those obtained in the hysteresis curves, Hc = 246.20 and 254.20 Oe. While sample of KOH at nominal 5 mol% Co shows a spread horizontal distribution with an average value ~250 Oe, similar to value obtained by hysteresis curves, Hc = 235.30 Oe.

The FORC diagram discriminates between different magnetic behaviors, mixtures of grains with variable domain states (i.e. size distribution of the particles) and identifies the presence or absence of magnetostatic interactions due to grains with different domain structures and interactions plotted in different parts of the FORC [15,16]. In this respect, it is seen that NaOH Co-doped samples present different magnetic characteristic than KOH Co-doped samples. The nominal 5 mol% Co-doped BT shows an ill-defined coercivity distribution (contour distribution) which would indicate that ferromagnetic behavior is not significant, with no clear identification of magnetic grain size. On the other hand, the 1 and 3 mol% Co-doped BT samples present mixing of the contour distributions. Both present a coercivity distribution with $Hc > 0$ and $Hu > 0$ and parallel to the H_{cf} axis, and another one close to the origin with intermediate vertical spread. This arrangement suggests a SD magnetic grain size with lower PSD magnetic domain in both Co-doped samples. In the case of the KOH Co-doped samples, it is observed that the nominal 5 mol% exhibits a distribution very close to the origin with a small vertical spread but large spread along the horizontal axis. This suggest a SP magnetic grain size, in agreement with the proximity to SD + 10 nm SP mixing curve evidenced in the Day-Dunlop diagram, unlike its NaOH counterpart which

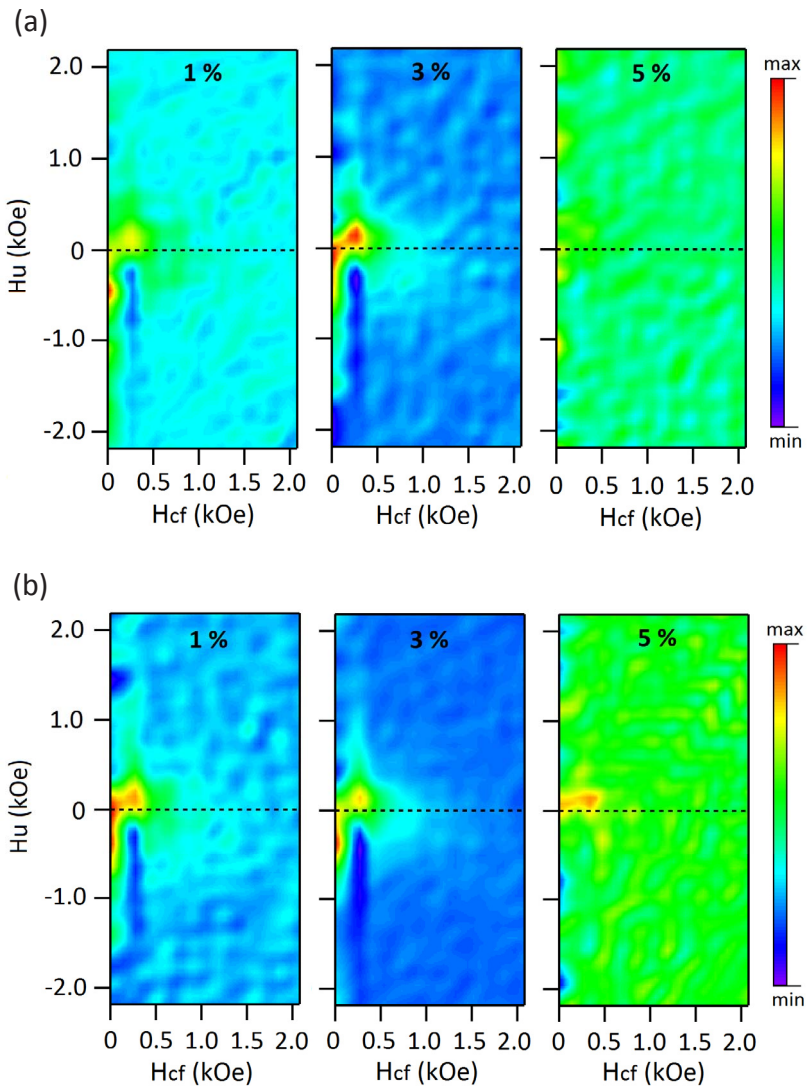

Fig. 9. FORC diagrams of the BT nanoparticles prepared with (a) NaOH and (b) KOH, doped with different content of Co: 1%, 3% and 5 mol%.

is plotted farther from the curve. For KOH at nominal 1 and 3 mol% Co doped samples, a broad coercitivity distribution is observed in the *Hcf* axis and close to the origin with a vertical spread. These characteristics suggest a ferromagnetic behavior controlled by a SD magnetic domain size with low magnetic interaction. However, a more horizontally spread coercitivity distribution with broad vertical spread is also observed, which could represent a PSD magnetic domain size. In the nominal 1 mol% Co-doped sample a higher density near to the origin is also observed, which can infer a greater SD magnetic grain size presence over the PSD size.

4. Conclusions

Co-doped BT compounds with different compositions using two different bases (NaOH and KOH) were examined. Different chemical and magnetic properties were obtained depending on the base used during the synthesis of the compound. Results from XPS and XRD reveal the presence of Co^{2+} and the possible presence of Co^{3+} as a mixture of oxidation states of cobalt in the Co-doped BT compounds. Our results suggest that Co^{2+} replaces the Ti^{4+} sites at low concentration (nominal 1 and 3 mol%), whereas both sites, Ba^{2+} and Ti^{4+}, may be substituted by Co^{3+} ions when the concentration increases (nominal 5 mol%). Raman spectra showed that with increasing Co, the intensity of the bands associated with tetragonal perovskite structure decrease. This is caused by the tetragonal-to-cubic phase transition from BT at Co-doped BT and is consistent with the effect observed by X-ray diffraction analysis.

Finally, we propose that there is a correlation between the hysteresis loop, the Day-Dunlop diagram and the FORC Diagrams, and that they describe sample behavior very well as a whole. All of the samples exhibited a paramagnetic and ferromagnetic component, except for the sample synthesized in KOH doped at nominal 1 mol%, where, apart from the ferromagnetic contribution, there was only a small diamagnetic contribution. The contribution of the paramagnetic and ferromagnetic behavior seems to be closely linked to the content of Co. The nominal 5 mol% doped samples synthesized in both NaOH and KOH present mainly a contribution of paramagnetic materials on ferromagnetic, which may be due to the fact that Ba^{2+} and Ti^{4+} are substituted by Co^{3+}, the more oxidized phase of Co^{2+}. Additionally, this ionic substitution generates a small lattice distortion which could be related to the SP magnetic domains component shown through Day-Dunlop and FORC diagrams. Samples doped at nominal 1 mol% Co in NaOH and at nominal 3 mol% in KOH tend to have a paramagnetic behavior over a ferromagnetic behavior, while samples doped at nominal 3 mol% Co in NaOH and at nominal 1 mol% in KOH tend to have a ferromagnetic behavior over the paramagnetic behavior.

The different samples present a mixture of magnetic domains between PSD, SD and SP. This is due to Co^{2+} replacing the Ti^{4+} sites at

low concentrations of Co, and could be explained by crystalline aggregates formed by different sizes of magnetic grains. According to this study, the particles that exhibit the best magnetic characteristics, in terms of magnetic interaction and magnetic grain size, are those synthesized in NaOH doped at nominal 3 mol%, and those synthesized in KOH doped at nominal 1 mol%.

Acknowledgments

This work has been partially financed by:Proyecto Basal CEDENNA FB0807, Proyecto Anillo ACT 1204 and 1409. H.P and N.B acknowledgments support CONICYT Doctoral Nacional No: 21150393 and 21141190. D.E. Diaz-Droguett thanks to Fondecyt project 11130555. S. Fuentes thanks to Fondequip project EQM140044.

References

[1] Y. Li, Y. Yaodong, W. Zhiguang, X. Zengping, L. Jiefang, D. Viehland, J. Mater. Sci. 44 (2009) 5080–5086.
[2] N. Sharma, A. Gaur, U.K. Gaur, Ceram. Int. 40 (2014) 16441–16448.
[3] L.W. Martin, Y.H. Chu, R. Ramesh, Mater. Sci. Eng. 68 (2010) 89–94.
[4] L. Da-Yong, L. Zhanga, S. Xiu-Yun, Ceram. Int. 39 (2013) 6369–6377.
[5] T. Sareein, P. Baipaywad, W. Chaiammad, A. Ngamjarurojan, S. Ananta, X. Tan, R. Yimnirun, Curr. Appl. Phys. 11 (2011) S90–S95.
[6] F. Yang, Y. Zhou, M. Tang, F. Liu, Y. Ma, X. Zheng, W. Zhao, H. Xu, Z. Sun, J. Phys. D: Appl. Phys. 42 (2009) (2010) 072004–72007.
[7] D.P. Dutta, M. Roy, N. Maiti, A.K. Tyagi, Phys. Chem. Chem. Phys. 18 (2016) 9758–9769.
[8] H. Zhai, J. Wang, T. Zhang, L. Zheng, H. Luo, H. Li, J. Yang, H. Liu, J. Su, Curr. Appl. Phys. 16 (2016) 686–692.
[9] U. Chaimongkon, A. Thongtha, T. Bongkarn, Curr. Appl. Phys. 11 (2011) S70–S76.
[10] R. Mangalam, N. Ray, U. Waghmare, A. Sundaresan, C.N.R. Rao, Solid State Commun. 149 (2009) 1–4.
[11] H. Lemziouka, R. Moubah, F.Z. Rachid, Y. Jouane, E.K. Hlil, M. Abid, H. Lassri, Ceram. Int. 42 (2016) 19402–19410.
[12] H. Liu, B. Cao, J.C. O'Connor, J. Magn. Magn. Mater 322 (2010) 790–797.
[13] H. Li, L. Xue, Y. Yan, J. Alloys Compd. 611 (2014) 38–45.
[14] H. Nakayama, H. Katayama-Yoshida, Jpn. J. Appl. Phys. 40 (2001) L1355–L1361.
[15] C.R. Pike, J. Appl. Phys. 85 (9) (1999) 6660–6668.
[16] A.P. Roberts, C.R. Pike, K.L. Verosub, J. Geophys. Res. 105 (B12) (2000) 28461–28469.
[17] S. Alikhanzadeh-Arani, M. Almasi-Kashi, A. Ramazani, Curr. Appl. Phys. 13 (4) (2013) 664.
[18] E. De Biasi, J. Curiale, R.D. Zysler, J. Magn. Magn. Mater 419 (2016) 580–589.
[19] G. Bertotti, Hysteresis in Magnetism, Academic Press, NY, USA, 1998.
[20] R.J. Harrison, J.M. Feinberg, Geochem. Geophys. Geosyst. 9 (2008) 5–11.
[21] M.S. Salem, P. Sergelius, R.M. Corona, J. Escrig, D. Gorlitz, K. Nielsch, Nanoscale 5 (2013) 3941–3950.
[22] S. Nasser, Appl. Surf. Sci. 157 (2000) 14–21.
[23] D. Ehre, H. Cohen, V. Lyahovitskaya, L. Lubomirsky, Phys. Rev. B 77 (2008) 184106–184116.
[24] C. Norman, C. Leach, J. Memb, Sci 382 (2011) 158–165.
[25] J. Jung, D. Edwards, J. Solid State Chem. 184 (2011) 2238–2245.
[26] S. Fuentes, E. Chávez, L. Padilla-Campos, D.E. Diaz-Droguett, Ceram. Int. 39 (2013) 8823–8831.
[27] S. Fuentes, F. Cespedes, L. Padilla-Campos, D.E. Diaz-Droguett, Ceram. Int. 40 (2014) 4975–4982.
[28] R.D. Shannon, Acta Cryst. A 32 (1976) 751–758.
[29] B. Cui, P. Yu, J. Tian, Z. Chang, Mater. Sci. Eng. B 133 (2006) 205–213.
[30] S. Fuentes, R.A. Zárate, E. Chávez, P. Muñoz, M. Ayala, R. Espinoza, J. Alloys Compd. 505 (2010) 568–574.
[31] G. Busca, V. Buscaglia, M. Leoni, P. Nanni, Chem. Mater. 6 (1994) 955–961.
[32] L. Tauxe, Paleomagnetic Principles and Practice, Kluwer Academic Publishers, Dordrecht, 1998, pp. 299–309.
[33] R. Day, M. Fuller, V.A. Schmidt, Phys. Earth Planet. Inter. 13 (1977) 260–269.
[34] D.J. Dunlop, J. Geophys. Res. 107 (B3) (2002) 2056, http://dx.doi.org/10.1029/2001JB000486.
[35] D.J. Dunlop, J. Geophys. Res. 107 (2002), http://dx.doi.org/10.1029/2001JB000487.
[36] M.E. Evans, F. Heller, Environmental Magnetism: Principles and Applications of Enviromagnetics, Elsevier Science, USA, 2003.
[37] W. Zhang, H. Li, W. Pan, J. Mater. Sci. 47 (2012) 8216–8223.
[38] L. Clime, S. Zhao, P. Chen, F. Normandin, H. Roberge, T. Veres, Nanotechnology 18 (2007) 435709–435716.
[39] C.R. Pike, A. Fernandez, J. Appl. Phys. 85 (1999) 6668–6675.
[40] C.R. Pike, Phys. Rev. B 68 (2003) 104424–104431.
[41] C.R. Pike, C.A. Ross, R.T. Scalettar, G. Zimanyi, Phys. Rev. B 71 (2005) 134407–134418.